

TOPICAL REVIEW

The Slater–Koster tight-binding method: a computationally efficient and accurate approach

To cite this article: D A Papaconstantopoulos and M J Mehl 2003 *J. Phys.: Condens. Matter* **15** R413

View the [article online](#) for updates and enhancements.

You may also like

- [THE CARNEGIE-IRVINE GALAXY SURVEY. III. THE THREE-COMPONENT STRUCTURE OF NEARBY ELLIPTICAL GALAXIES](#)

Song Huang, , Luis C. Ho et al.

- [Flat band properties of twisted transition metal dichalcogenide homo- and heterobilayers of \$\text{MoS}_2\$, \$\text{MoSe}_2\$, \$\text{WS}_2\$ and \$\text{WSe}_2\$](#)

V Vitale, K Atalar, A A Mostofi et al.

- [High-precision angle sensor based on a Köster's prism with absolute zero-point](#)

V Ullmann, E Oertel and E Manske

TOPICAL REVIEW

The Slater–Koster tight-binding method: a computationally efficient and accurate approach

D A Papaconstantopoulos and M J Mehl

Center for Computational Materials Science, Naval Research Laboratory, Washington, DC, USA

E-mail: papacon@dave.nrl.navy.mil and mehl@dave.nrl.navy.mil

Received 26 November 2002, in final form 10 January 2003

Published 3 March 2003

Online at stacks.iop.org/JPhysCM/15/R413**Abstract**

In this article we discuss the Slater–Koster (SK) tight-binding (TB) method from the perspective of our own developments and applications to this method. We first present an account of our work in constructing TB Hamiltonians and applying them to a variety of calculations which require an accurate representation of the electronic energy bands and density of states. In the second part of the article we present the Naval Research Laboratory TB method, wherein we demonstrate that this elaborate scheme can accurately account for both the band structure and total energy of a given system. The SK parameters generated by this method are transferable to other structures and provide the means for performing computationally demanding calculations of fairly large systems. These calculations, including molecular dynamics, are of comparable accuracy to first-principles calculations and three orders of magnitude faster.

Contents

1. Introduction	414
2. Formalism of the tight-binding method	415
3. Fitting of band structures	417
3.1. Single-element materials	418
3.2. Binary compounds	419
3.3. Ternary compounds	420
3.4. High-temperature superconductors	421
4. The NRL tight-binding method	422
4.1. The tight-binding parameters—elemental systems	423
4.2. The tight-binding parameters—multi-component systems	425
5. Equation of state	426
6. Elastic constants	427
7. Phonon frequencies	428
8. Vacancies	430

9. Surfaces	431
10. Stacking faults and ductility	432
11. Semiconductors	434
12. Molecular dynamics	434
13. Magnetism	435
14. Binary compounds	436
Acknowledgments	437
References	438

1. Introduction

The classic paper of Slater and Koster (SK) [1] proposed a modified linear combination of atomic orbitals (LCAO) method to interpolate the results of first-principles electronic structure calculations. As they noted, at the time (1954) it was computationally impossible to directly evaluate the large number of integrals occurring in the LCAO method. However, since this approach shows all of the correct symmetry properties of the energy bands as well as providing solutions of the single-particle Schrödinger equation at arbitrary points in the Brillouin zone, they suggested that these integrals be considered as adjustable constants determined from the results of other, more efficient, calculations.

Although the continuous development of computers has eliminated some of the initial reasons for developing this interpolation scheme for the LCAO method, it has evolved into a powerful approach for calculating the total energy, electronic energy bands, and electronic densities of states for arbitrary systems. Over the last 40 years there have been numerous applications of this method, which has been pursued in a variety of problems, following different philosophies and placing different levels of emphasis on the required level of accuracy.

In addition to the original SK paper, the interested reader should consult the review article by Nussbaum [2] for details of the formalism of the SK approach. An early review of applications of the tight-binding (TB) method may be found in the articles in volume 35 of *Solid State Physics* [3–6]. A good account of TB theory can be found in Harrison’s book [7]. He developed a ‘universal’ set of TB parameters which is very useful for making approximate calculations and very important for obtaining a basic understanding of band structures. We have also covered some aspects of TB theory in an earlier review [8].

In this paper we first present a summary of the SK theory in section 2, and then concentrate on presenting an account of our own contributions to the SK method. Our emphasis is on an implementation of the method which accurately reproduces first-principles data in a computationally efficient way, while avoiding simplifications that may take us into a regime where we would obtain only a qualitative account of the electronic structure. While our work is based on constructing TB Hamiltonians by fitting to first-principles calculations, there have been efforts to derive these Hamiltonians from density functional theory [9].

The present work reflects two phases. The first refers to applications of the SK method which are based on fitting only the electronic energy bands and density of states (DOS). The most comprehensive source of this work is [10]. The second phase is represented by the Naval Research Laboratory tight-binding (NRL-TB) method [11, 12]. This approach includes total energy as well as energy bands in the fit, and uses distance- and environment-dependent SK parameters to provide transferability between different structures. The first phase is described in section 3. The NRL-TB model is described in section 4, with various applications in the following sections.

2. Formalism of the tight-binding method

The TB or SK formalism is an extension of Bloch's original LCAO method [13]. Consider a periodically replicated unit cell, where the lattice vectors are denoted as \mathbf{R}_m , with a set of atoms i located at positions \mathbf{b}_i in each unit cell. Associated with each atom is a set of atomic-like orbitals $\phi_{i\alpha}$, where α denotes both the orbital and angular quantum numbers of the atomic state. In general, orbitals which are on different atoms are not orthogonal. In this case, we may use Löwdin's method [14] to construct a set of wavefunctions $\psi_{i\alpha}$ which have symmetry properties similar to those of the corresponding $\phi_{i\alpha}$, but are orthogonal:

$$\int \psi_{i\alpha}^*(\mathbf{r} - \mathbf{R}_m - \mathbf{b}_i) \psi_{j\beta}(\mathbf{r} - \mathbf{R}_n - \mathbf{b}_j) d^3r = \delta_{ij} \delta_{mn}. \quad (1)$$

As in standard LCAO calculations and in the Hohenberg–Kohn–Sham density functional theory (DFT) formalism [15, 16], we now assume that the system can be described by a set of non-interacting single-particle wavefunctions which obey Fermi statistics. Following Bloch's theorem, these wavefunctions can be written in the form

$$\Psi_{kia}(\mathbf{r}) = N^{-1/2} \sum_n \exp(i\mathbf{k} \cdot \mathbf{R}_n) \psi_{i\alpha}(\mathbf{r} - \mathbf{R}_n - \mathbf{b}_i), \quad (2)$$

where \mathbf{k} is the Bloch wavevector and N is the number of unit cells in the sum. The solution to Schrödinger's equation for wavevector \mathbf{k} then requires the diagonalization of the Hamiltonian matrix using the basis functions (2). Since the Hamiltonian H has the periodicity of the lattice, this basis will block-diagonalize the Hamiltonian, with each block having a single value of \mathbf{k} . Within one of these blocks, the matrix elements can be written in the form

$$H_{i\alpha,j\beta}(\mathbf{k}) = \sum_n \exp(i\mathbf{k} \cdot \mathbf{R}_n) \int \psi_{i\alpha}^*(\mathbf{r} - \mathbf{R}_n - \mathbf{b}_i) H \psi_{j\beta}(\mathbf{r} - \mathbf{b}_j) d^3r, \quad (3)$$

where we have used the translation symmetry of the lattice to remove one of the sums over the lattice vectors \mathbf{R} .

The Hamiltonian H includes a single-particle potential, which we may write, without approximation, as

$$V(\mathbf{r}) = \sum_{nk} V_k(\mathbf{r} - \mathbf{R}_n - \mathbf{b}_k), \quad (4)$$

where the potential V_k is centred on the k th atom and vanishes at some distance away from that atom. If we substitute this expression and the wavefunction expansion equation (2) into (3), then each term of the integral has a contribution from one of three regions: the regions centred around the two atomic-like wavefunctions $\psi_{i\alpha}$ and $\psi_{j\alpha}$, and the region centred around the potential at \mathbf{b}_k . This leads to a classification of the integrals into four categories:

- (i) If all three locations are on the same atom, this is an *on-site* integral.
- (ii) If the location of the potential is the same as the location of one of the wavefunctions, while the other wavefunction is at a separate location, this is a *two-centre* integral.
- (iii) If the wavefunctions and the potential are all located at different sites, this is a *three-centre* integral.
- (iv) The fourth category occurs when the wavefunctions both come from the same site but the potential is on a different site. This category shares features with both the two-centre and three-centre integrals but is actually a local environment or crystal field correction to the on-site terms. This category was ignored by SK, but the formalism for its use was later developed for s and p orbitals by Mercer and Chou [17] and extended to d orbitals by Cohen *et al* [18]. We will not consider this type of integral further in this paper.

Following SK, we now assume that the potentials $V_k(\mathbf{r})$ are spherically symmetric. Then the wavefunctions ψ and ϕ can be specified by the usual angular momentum quantum numbers, and the on-site integrals only contribute to the diagonal elements of the Hamiltonian. We further assume that the three-centre integrals can be neglected compared to the two-centre integrals. This is not strictly true [1, 10], but it considerably simplifies the method, and in many cases leads to accurate predictions of the electronic structure and total energy of a system, as we shall see. In this *two-centre approximation* the integrals in (3) depend only on the displacement \mathbf{u} between the two atoms, and have the form

$$H_{\alpha\beta}^{ij}(\mathbf{u}) = \int \psi_{i\alpha}^*(\mathbf{r} - \mathbf{u}) H_{2c} \psi_{j\beta}(\mathbf{r}) d^3r, \quad (5)$$

where H_{2c} is the two-centre part of the Hamiltonian, i.e., the kinetic energy operator and a spherically symmetric potential centred on atom i or on atom j . These terms depend on the orientation of \mathbf{u} , the magnitude of the separation between atoms ($u = |\mathbf{u}|$), and the angular momenta contained in the quantum numbers α and β . If we restrict the atomic orbitals ϕ_i to s, p, and d angular momenta, then each term of equation (5) can be written in terms of **14 SK parameters**. In our notation these will be denoted as $H_{aby}(u)$, where a and b specify the angular momenta of the orbitals (s, p, d), and $\gamma = \sigma, \pi, \delta$ specifies the component of the angular momentum relative to the direction \mathbf{u} . In the case where the two atoms are identical, four pairs of the SK parameters are related by symmetry, giving ten independent parameters. We should note that the matrix elements are short range: if the wavefunctions $\psi_{i\alpha}(\mathbf{r} - \mathbf{u})$ and $\psi_{j\beta}(\mathbf{r})$ do not appreciably overlap, then the integral equation (5) will vanish.

In the SK method we replace the on-site and two-centre integrals $H_{aby}(u)$ by parameters which are chosen to reproduce the first-principles single-particle band structure of a standard crystal or set of crystals. In the original SK work these parameters were determined by fitting to first-principles band structures at high-symmetry points. The parameters were then used as interpolation parameters to describe the band structure throughout the Brillouin zone. However, as we shall see below, properly chosen SK parameters are frequently transferable from one structure to another. They can be used to describe structures which are not in the original database.

Mattheiss [19] modified this two-centre TB method to use *non-orthogonal* orbitals, i.e., omitting the Löwdin transformation of the atomic orbitals ϕ into orthogonal orbitals ψ . The basis functions equation (2) are then replaced by the functions

$$\Phi_{kia}(\mathbf{r}) = N^{-1/2} \sum_n \exp(i\mathbf{k} \cdot \mathbf{R}_n) \phi_{i\alpha}(\mathbf{r} - \mathbf{R}_n - \mathbf{b}_i). \quad (6)$$

Since these are no longer orthogonal, the problem of diagonalizing the Schrödinger equation is transformed into a generalized eigenvalue problem, involving the Hamiltonian matrix elements of equation (3), with the $\psi_{i\alpha}$ replaced by the corresponding $\phi_{i\alpha}$, and an overlap matrix

$$S_{i\alpha,j\beta}(\mathbf{k}) = \sum_n \exp(i\mathbf{k} \cdot \mathbf{R}_n) \int \phi_{i\alpha}^*(\mathbf{r} - \mathbf{R}_n - \mathbf{b}_i) \phi_{j\beta}(\mathbf{r} - \mathbf{b}_j) d^3r. \quad (7)$$

Since the matrix (7) does not include a Hamiltonian term, it can be exactly decomposed into on-site terms (which form a diagonal matrix if the ϕ are truly atomic-like) and two-centre terms,

$$S_{\alpha\beta}^{ij}(\mathbf{u}) = \int \phi_{i\alpha}^*(\mathbf{r} - \mathbf{u}) \phi_{j\beta}(\mathbf{r}) d^3r, \quad (8)$$

which have the same symmetry as the corresponding two-centre Hamiltonian matrix elements (5). These two-centre terms can be parametrized in the same way as the corresponding

Hamiltonian, into terms denoted as $S_{ab\gamma}$. This introduces another 14 SK parameters (ten if the atoms are identical) for systems described in terms of s, p, and d orbitals.

The use of the non-orthogonal formalism has two advantages. The most obvious is that the additional parameters make it easier to fit band structures in a large database. A less obvious advantage comes from the nature of the Löwdin transformation of the atomic orbitals ϕ into orthogonal wavefunctions ψ . By necessity the ψ have a longer range than the atomic wavefunctions. Use of the atomic wavefunctions means that the two-centre SK parameters in equations (5) and (8) can have a shorter range, usually only a few nearest-neighbour shells. Thus the non-orthogonal matrix elements sample only the local environment of each atom, making the development of transferable TB parameters easier.

3. Fitting of band structures

In the early works the aim with the SK scheme [1] was to use it as an interpolation method to efficiently produce the eigenvalue spectrum $\varepsilon_n(\mathbf{k})$ at a large number of \mathbf{k} -points for a given structure. This procedure was very useful for the determination of the Fermi surface and the DOS. The approach proceeds as follows: for a given system for which first-principles calculations are available one decides which orbitals to include in the Hamiltonian. For example for transition metals one uses s, p, and d orbitals while for semiconductors such as Si it suffices to use the s and p orbitals. The next question is how many neighbours (for crystals, neighbour shells) to include in the Hamiltonian. We have found that including only the first neighbours is not enough for an accurate fit. The inclusion of second and often third neighbours is necessary. There are, in general, four different forms of a SK Hamiltonian, corresponding to various approximations described in the previous section. These are the following: (a) three-centre orthogonal, (b) three-centre non-orthogonal, (c) two-centre orthogonal, and (d) two-centre non-orthogonal. The two-centre approximation reduces the number of SK parameters and has the advantage that the parameters have a form independent of the crystal structure, which makes them easily transferable from one structure to another. For this reason the two-centre parameters are more frequently used, although a three-centre parametrization is more accurate. A non-orthogonal Hamiltonian is preferable on physical grounds, and is also more accurate since it employs almost twice as many SK parameters. However, the simplicity of an orthogonal Hamiltonian is often an important advantage, as for example in coherent potential approximation (CPA) calculations [20], where it considerably simplifies the formalism.

The determination of the SK parameters is usually done by a least-squares procedure in which one tries to minimize the eigenvalue difference $\delta\varepsilon_i$ between first-principles and SK values for a large number of \mathbf{k} -points. For the cubic crystals we generally use a regular \mathbf{k} -point mesh which has 89, 55, or 35 \mathbf{k} -points in the irreducible Brillouin zone for fcc, bcc, and simple cubic (sc) lattices, respectively. We use \mathbf{k} -point meshes with similar densities for other structures, e.g., hcp. Another issue which must be considered is the number of bands per \mathbf{k} -point. The procedure that we follow is to fit all the occupied states but also include empty states. For the transition metals in particular we fit six bands for all \mathbf{k} -points and we include the bands 7–9 only for the four high-symmetry points (Γ , X, L and W for fcc; Γ , H, N and P for bcc). This ensures that the SK parameters originating from transition metal p orbitals maintain sensible values. For covalent semiconductors (e.g., diamond structure materials) where only the s and p orbitals are included, one fits a total of eight bands (four valence and four conduction). The fit of the conduction band is not very accurate but the valence bands are very well fitted and the gap is reproduced adequately. For the monatomic metals we have RMS deviations from the first-principles results typically ranging from 1 mRyd for non-orthogonal Hamiltonians to 5 mRyd for orthogonal. For the semiconductors (Si and Ge) the RMS errors are 8 and

Table 1. Block-diagonalization of the 9×9 TB Hamiltonian at high-symmetry points of the fcc lattice. The ordering of the states is s, p(x), p(y), p(z), d(yz), d(zx), d(xy), d($x^2 - y^2$), d($3z^2 - r^2$).

State	k -point	Matrix	Degeneracy
Γ_1		$[H_{11}]$	1
Γ_{12}	$(0, 0, 0)$	$[H_{88}]$	2
Γ_{15}		$[H_{22}]$	3
Γ'_{25}		$[H_{55}]$	3
X_1		$\begin{bmatrix} H_{11} & H_{19} \\ H_{19}^* & H_{99} \end{bmatrix}$	1
X_2		$[H_{88}]$	1
X_3	$\left(0, 0, \frac{2\pi}{a}\right)$	$[H_{77}]$	1
X'_4		$[H_{44}]$	1
X_5		$[H_{55}]$	2
X'_5		$[H_{22}]$	2
L_1		$\begin{bmatrix} H_{11} & \frac{1}{\sqrt{3}}[H_{15} + H_{16} + H_{17}] \\ \frac{1}{\sqrt{3}}[H_{15}^* + H_{16}^* + H_{17}^*] & \frac{1}{3} \left\{ H_{55} + H_{66} + H_{77} + 2(H_{56} + H_{57} + H_{67}) \right\} \end{bmatrix}$	1
L'_2	$\left(\frac{\pi}{a}, \frac{\pi}{a}, \frac{\pi}{a}\right)$	$[(1/3)(H_{22} + H_{33} + H_{44}) + (2/3)(H_{23} + H_{24} + H_{34})]$	1
L_3		$\begin{bmatrix} (1/2)[H_{55} - 2H_{56} + H_{66}] & (1/\sqrt{2})[H_{58} - H_{68}] \\ (1/\sqrt{2})[H_{58}^* - H_{68}^*] & H_{88} \end{bmatrix}$	2
L'_3		$[(1/2)(H_{22} - 2H_{23} + H_{33})]$	2
W_1	$\left(0, \frac{2\pi}{a}, \frac{\pi}{a}\right)$	$\begin{bmatrix} H_{11} & H_{19} \\ H_{19}^* & H_{99} \end{bmatrix}$	1
W'_2		$\begin{bmatrix} H_{44} & H_{48} \\ H_{48}^* & H_{88} \end{bmatrix}$	1
W'_1		$[H_{66}]$	1
W_3	$\left(0, \frac{\pi}{a}, \frac{2\pi}{a}\right)$	$\begin{bmatrix} H_{22} & H_{27} \\ H_{27}^* & H_{77} \end{bmatrix}$	2

30 mRyd for non-orthogonal and orthogonal Hamiltonians, respectively, when including six bands in the fit (four valence and the lowest two conduction bands). Some improvement in the conduction band could be achieved by including Si or Ge d orbitals [21].

An important issue in obtaining high-quality results in the SK method is the block-diagonalization of the Hamiltonian. This procedure avoids the possibility of incorrectly assigning the symmetry and angular momentum character of states. The reader can find the details of this technique in the book by Papaconstantopoulos [10]. As an example, tables 1 and 2 show how the 9×9 matrix reduces to linear or quadratic equations for the high-symmetry points in the fcc and bcc lattices, respectively.

3.1. Single-element materials

Reference [10] is a comprehensive source of SK parameters, including orthogonal and non-orthogonal Hamiltonians and both two- and three-centre parameters. This book includes all categories of SK parameters for 53 of the elements in the periodic table. Figures show the energy bands and electronic DOS for both cubic and hexagonal materials. Reference [10] also contains technical details and computer programs, as well as short discussions of trends and characteristics of band structures across the periodic table.

Table 2. Block-diagonalization of the 9×9 TB Hamiltonian at high-symmetry points of the bcc lattice. The ordering of the states is s, p(x), p(y), p(z), d(yz), d(zx), d(xy), d($x^2 - y^2$), d($3z^2 - r^2$).

State	k -point	Matrix	Degeneracy
Γ_1		$[H_{11}]$	1
Γ_{12}	$(0, 0, 0)$	$[H_{88}]$	2
Γ_{15}		$[H_{22}]$	3
Γ'_{25}		$[H_{55}]$	3
H_1		$[H_{11}]$	1
H_{12}	$\left(0, 0, \frac{2\pi}{a}\right)$	$[H_{88}]$	2
H_{15}		$[H_{22}]$	3
H'_{25}		$[H_{77}]$	3
N_1	$\left(\frac{\pi}{a}, \frac{\pi}{a}, 0\right)$	$\begin{bmatrix} H_{11} & H_{17} & H_{19} \\ H_{17}^* & H_{77} & H_{79} \\ H_{19}^* & H_{79}^* & H_{99} \end{bmatrix}$	1
N_4		$[H_{88}]$	1
N'_1		$[(1/2)(H_{33} + 2H_{34} + H_{44})]$	1
N_2		$[(1/2)(H_{66} - 2H_{67} + H_{77})]$	1
N_3	$\left(0, \frac{\pi}{a}, \frac{\pi}{a}\right)$	$[(1/2)(H_{66} + 2H_{67} + H_{77})]$	1
N'_3		$[H_{22}]$	1
N'_4		$[(1/2)(H_{33} - 2H_{34} + H_{44})]$	1
P_1		$[H_{11}]$	1
P_3	$\left(\frac{\pi}{a}, \frac{\pi}{a}, \frac{\pi}{a}\right)$	$[H_{88}]$	2
P_4		$\begin{bmatrix} H_{22} & H_{26} \\ H_{26}^* & H_{66} \end{bmatrix}$	3

It should be emphasized that the work in [10], like the work described in sections 3.2 and 3.3 below, concentrates on fitting the SK parameters to the band structure of the ground state of each material. The issues of transferability of the SK parameters to other structures, differing in volume or symmetry, and the inclusion of total-energy calculations are taken up in section 4, where we describe the latest NRL-TB method.

3.2. Binary compounds

The SK interpolation scheme has also been applied to binary compounds. The size of the secular equation in this case will depend upon the number of atoms in the unit cell and the number of orbitals that we take for each atom. For example in a typical B2 (CsCl) structure material such as TiNi, which involves two transition metals, we utilize an 18×18 Hamiltonian that includes s, p, and d orbitals on both sites. Figure 1 shows a comparison of augmented plane wave (APW) [23, 24] and SK energy bands for B2 (CsCl structure) TiNi. The agreement for the first 11 bands, which includes both the Ti and Ni d bands, is impressive. More details on these calculations, including the block-diagonalization procedure, are given in [22]. In materials such as the B1 (NaCl) structure hydrides, e.g. PdH, one only incorporates the 1s H orbital, and so a 10×10 Hamiltonian is needed [25]. For like-structured carbides and nitrides we include 9spd orbitals from the transition metal and the 4sp orbitals of C or N, for a Hamiltonian of dimension 13×13 . As an example, figure 2 shows the APW and SK band structures of B1-phase NbC. The first nine bands are so well fitted that the solid and broken curves cannot

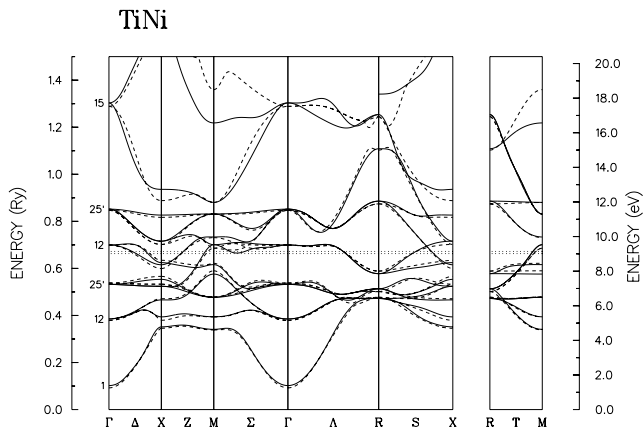


Figure 1. Comparison of the first-principles APW band structure of B2 (CsCl structure) TiNi (solid curves) with the band structure calculated using the SK parametrization (broken curves) of [22].

be distinguished. A complete set of SK parameters, band structures, and DOS figures for the paramagnetic NaCl structure hydrides, carbides, nitrides, and oxides can be found in our electronic structure database¹. We caution the reader interested in using our SK parameters to utilize our programs, because changes in the signs of the SK parameters often occur. We are not limited to fitting APW band structures. Figure 3 shows the SK band structure of GaAs compared to an empirical pseudopotential calculation. The valence band is fitted perfectly while the conduction band is not quite so good, as is common in calculations using only s and p orbitals. We have also applied this method to other two-component structures such as fluorite (CaF_2), where we have used an 11×11 matrix within the CPA to study the electronic structure of disordered transition metal dihydrides [26]. Of course, in the CaF_2 structure the secular matrix can be 27×27 if all orbitals are included. Similarly, the Cu_3Au structure would involve a 36×36 matrix.

3.3. Ternary compounds

Our approach has also been extended to the cubic perovskite ($E2_1$) structure ABC_3 where the Hamiltonian size is in general 45×45 . In practice we have confined ourselves to oxides, which reduces the matrix size to no more than 30×30 . We have applied this method to the following systems: BaSnO_3 , BaSbO_3 , BaPbO_3 , BaBiO_3 , KBiO_3 , SrTiO_3 , LaMnO_3 , and SrRuO_3 . In these systems we have reduced the size of our Hamiltonian depending on our observations on the participation of various orbitals in forming the band structure. For example the O s orbital does not contribute to the valence states and can be omitted in constructing the SK Hamiltonian. We also found that only the s orbital of Ba and the s and p orbitals of Pb need to be retained for the first four compounds. Details of these calculations are given in [27]. A comparison of APW and SK bands for SrTiO_3 is shown in figure 4. We note that the fit for this perovskite structure, with RMS errors of about 15 mRyd, is not as good as for the diatomic materials, where we had RMS errors averaging less than 5 mRyd.

For LaMnO_3 and SrRuO_3 we find accurate Hamiltonians constructed by utilizing only the d Mn and Ru orbitals and the O p orbitals. In addition, for the above manganites and

¹ The NRL electronic structure database is available online at <http://cst-www.nrl.navy.mil/es-access.html> (Registration is required.)

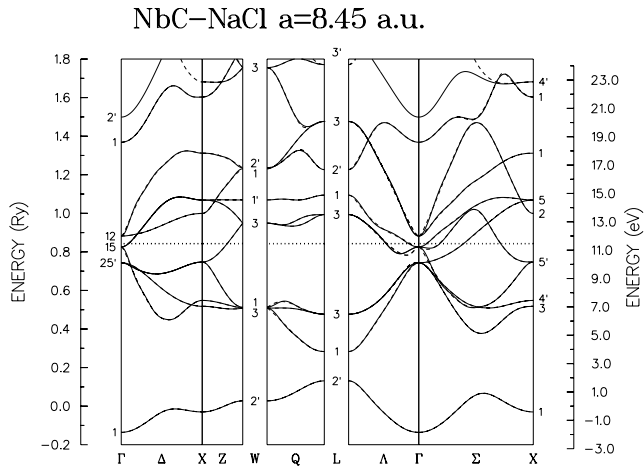


Figure 2. Comparison of the first-principles APW band structure of B1 (NaCl structure) NbC (solid curves) with the band structure calculated using an SK parametrization.

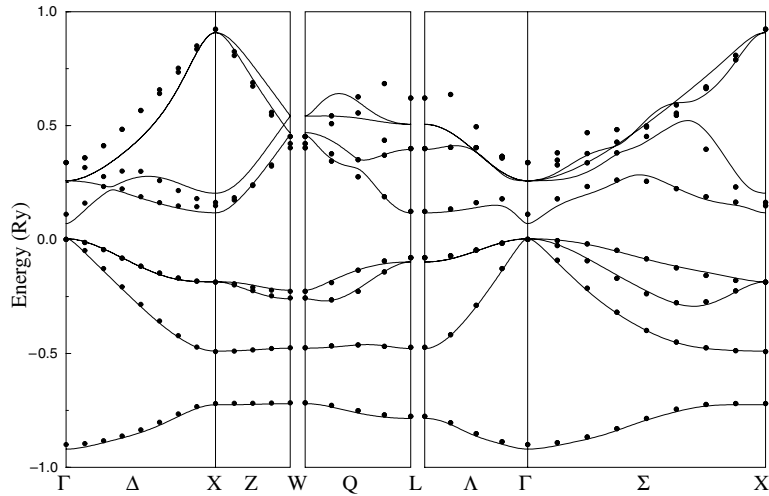


Figure 3. Comparison of an empirical pseudopotential band structure of GaAs (dots) to the band structure obtained by SK parametrization (solid curve).

ruthenates we were able to obtain good fits of the spin-polarized bands, with only the on-site SK parameters changing between the two spins. Details of these calculations may be found in [28] and [29]. We note that [29] presents a very accurate parametrization for the body-centred tetragonal structure of Sr_2RuO_4 and applies it to the calculation of the Hall coefficient.

3.4. High-temperature superconductors

We have also constructed accurate TB Hamiltonians for the high-temperature superconductors La_2CuO_4 and $\text{YBa}_2\text{Cu}_3\text{O}_7$ by fitting to full-potential linear augmented plane wave (LAPW) [30, 31] results. While other investigators have proposed simplified models based on isolated Cu–O planes, our approach accounts for the three-dimensional character of the

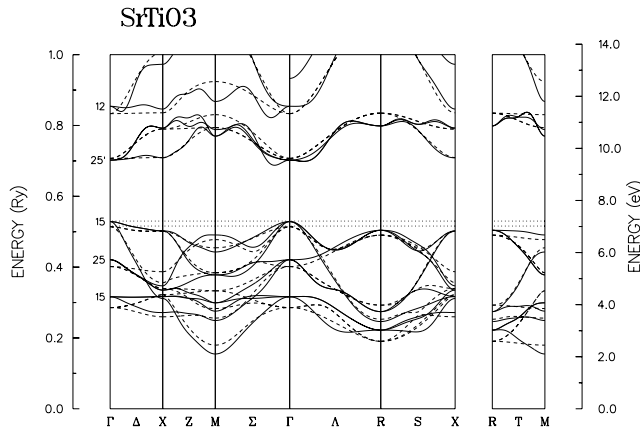


Figure 4. Comparison of the APW (solid curve) and SK (dashed curve) band structures of SrTiO_3 perovskite.

bands. These calculations support the hypothesis of a rigid band lowering of the Fermi level, ε_F , upon substitution of Ba for La in La_2CuO_4 . This, in turn, enhances $N(\varepsilon_F)$, the electron DOS at the Fermi level. The calculations also show that oxygen vacancies lower ε_F and raise $N(\varepsilon_F)$. Details are given in [32] and [33].

4. The NRL tight-binding method

Up to this point we have discussed TB parametrizations of the band structure alone. Total-energy information is not given by these calculations, although a band energy can be readily determined from the sum of the eigenvalues over the occupied states. However, in single-particle band theory this sum is only a partial contribution to the total energy. In the Kohn–Sham single-particle DFT ansatz [16], the total energy is given by

$$E = \int \frac{d^3k}{(2\pi)^3} \sum_n \varepsilon_n(k) + F[n(r)], \quad (9)$$

where the integral is over the first Brillouin zone, the sum is over occupied states, and $F[n(r)]$ is a functional of the density which includes the repulsion of the ionic cores, correlation effects, and part of the Coulomb interaction. Note that the value of the integral depends upon the choice of zero for the Kohn–Sham potential $v_{KS}(r)$ which generates the eigenvalue spectrum:

$$-\nabla^2 \psi_n(r) + v_{KS}(r) \psi_n(r) = \varepsilon_n \psi_n(r). \quad (10)$$

This choice is arbitrary. In many methods the potential is chosen such that the Fermi level is at zero energy. Since the width of the occupied states tends to increase with increasing pressure, the eigenvalue sum in (9) becomes more negative, and the function $F[n(r)]$ must be repulsive. However, first-principles band structure algorithms such as the APW [23, 24] or linearized augmented plane wave (LAPW) [30, 31] methods tend to choose the zero of the potential to be near the *bottom* of the occupied valence band. In this case, the eigenvalue sum increases with increasing pressure, i.e., it is repulsive, and $F[n(r)]$ must represent an attractive function.

In many TB methods it has become customary to make the first choice above and add a repulsive potential, representing $F[n(r)]$, to the band energy. This sum represents the total energy of the system. There are many variants of this approach with some of them resembling the embedded atom method (EAM) [34, 35]. We will only mention here the second-moment

approximation (SMA) because of our own work in this area. In our implementation of the SMA [36–38] we determine the potential by fitting to the volume dependence of the total energy computed by carrying out first-principles APW calculations instead of fitting to experimental quantities, as other workers do.

In the rest of this section will concentrate on the method developed at NRL by Cohen, Mehl, and Papaconstantopoulos [11, 12]. In this method we shift the potential v_{KS} in (10) by an amount

$$V_0 = F[n(\mathbf{r})]/N_e, \quad (11)$$

where N_e is the number of electrons in the unit cell. Then the total energy of the system is

$$\begin{aligned} E &= \int \frac{d^3k}{(2\pi)^3} \sum_n \varepsilon_n(\mathbf{k}) + F[n(\mathbf{r})] = \int \frac{d^3k}{(2\pi)^3} \sum_n \varepsilon_n(\mathbf{k}) + N_e V_0 \\ &= \int \frac{d^3k}{(2\pi)^3} \sum_n [\varepsilon_n(\mathbf{k}) + V_0]. \end{aligned} \quad (12)$$

If we now define a shifted eigenvalue,

$$\varepsilon'_n(\mathbf{k}) = \varepsilon_n(\mathbf{k}) + V_0, \quad (13)$$

then to get the total energy we just sum the shifted eigenvalues of the occupied states:

$$E = \int \frac{d^3k}{(2\pi)^3} \sum_n \varepsilon'_n(\mathbf{k}). \quad (14)$$

Note that V_0 depends upon the structure of the crystal, as well as the original method for determining the energy zero. As an aside, we note that the $\varepsilon'_n(\mathbf{k})$ are in some sense ‘universal’. That is, if any two band structure methods are sufficiently well converged, they will give the same total energy (9), and the eigenvalues derived from the two methods will differ by only a constant. Then the definition of V_0 for each method will be such that the shifted eigenvalues $\varepsilon'_n(\mathbf{k})$ are identical. Further insights into this procedure are given by McMahan and Klepeis [39]. This paper also contains a thorough extension of TB theory to include f orbitals.

In the NRL method, we construct a first-principles (LAPW or APW) database of eigenvalues $\varepsilon_n(\mathbf{k})$ and total energies E for several crystal structures at several volumes. (For example, for the transition metals we typically use five volumes each for both the fcc and bcc crystals.) We then find V_0 for each system, and shift the eigenvalues. Next, we attempt to find a set of parameters which will generate non-orthogonal, two-centre SK Hamiltonians which will reproduce the energies and eigenvalues in the database.

4.1. The tight-binding parameters—elemental systems

We assume that the on-site terms are diagonal and sensitive to the environment. For single-element systems we assign atom i in the crystal an embedded-atom-like ‘density’

$$\rho_i = \sum_j \exp(-\lambda^2 R_{ij}) F(R_{ij}), \quad (15)$$

where the sum is over all of the atoms j within a range R_c of atom i ; λ is our first fitting parameter, squared to ensure that the contributions are greatest from the nearest neighbours; and $F(R)$ is a cut-off function,

$$F(R) = \theta(R_c - R)/\{1 + \exp[(R - R_c)/\ell + 5]\}, \quad (16)$$

where $\theta(z)$ is the step function. Typically we take R_c between 10.5 and 16.5 Bohr (1 Bohr = 0.529 177 249 Å) and ℓ between 0.25 and 0.5 Bohr.

We then define the angular-momentum-dependent on-site terms by

$$h_{i\ell} = a_\ell + b_\ell \rho^{\frac{2}{3}} + c_\ell \rho^{\frac{4}{3}} + d_\ell \rho^2, \quad (17)$$

where $\ell = s, p$, or d . These $(a, b, c, d)_\ell$ form our next twelve (12) fitting parameters.

In some cases, notably that of vanadium [12], we have split the d on-site term into a term with t_{2g} symmetry (xy , yz , and zx orbitals) and a term with e_g symmetry ($x^2 - y^2$ and $3z^2 - r^2$ orbitals). This gives us an additional four parameters, raising the total on-site parameter count from 13 to 17. While this does improve the ability of the parametrization to describe cubic phases, it leads to problems in non-cubic phases such as hcp, where the t_{2g} - e_g splitting is meaningless. For most elements we therefore fit only to a single d on-site parameter. A better formulation would be to include crystal field effects in the formulation of the on-site terms in the manner of Mercer and Chou [17] and Cohen *et al* [18]. For an spd system there are ten such on-site parameters, many of which can be determined only by studying systems with very low symmetry. The philosophy of the NRL method is to find a good transferable set of parameters using only high-symmetry first-principles calculations. For this reason we have decided to include only the limited angular momentum dependence (17) in our database.

In the spirit of the two-centre approximation, we assume that the hopping integrals depend only upon the angular momentum dependence of the orbitals and the distance between the atoms. Slater and Koster [1] showed that all two-centre (spd) hopping integrals can then be constructed from ten independent parameters, the SK parameters, $H_{\ell\ell'\mu}$, where

$$(\ell\ell'\mu) = ss\sigma, sp\sigma, pp\sigma, pp\pi, sd\sigma, pd\sigma, pd\pi, dd\sigma, dd\pi, \text{ and } dd\delta. \quad (18)$$

We assume a polynomial \times exponential form for these parameters:

$$H_{\ell\ell'\mu}(R) = (e_{\ell\ell'\mu} + f_{\ell\ell'\mu} R + g_{\ell\ell'\mu} R^2) \exp(-h_{\ell\ell'\mu}^2 R) F(R), \quad (19)$$

where R is the separation between these atoms and $F(R)$ is the cut-off function (16). The parameters $(e_{\ell\ell'\mu}, f_{\ell\ell'\mu}, g_{\ell\ell'\mu}, h_{\ell\ell'\mu})$ constitute the next forty (40) fitting parameters.

Since this is a non-orthogonal calculation, we must also define a set of SK overlap functions. These represent the overlap between two orbitals separated by a distance R . They have the same angular momentum behaviour as the hopping parameters (18). We have used two different parametrizations for the overlap parameters. The first is identical in form to (19):

$$S_{\ell\ell'\mu}(R) = (p_{\ell\ell'\mu} + q_{\ell\ell'\mu} R + r_{\ell\ell'\mu} R^2) \exp(-s_{\ell\ell'\mu}^2 R) F(R). \quad (20)$$

The parameters $(p_{\ell\ell'\mu}, q_{\ell\ell'\mu}, r_{\ell\ell'\mu}, s_{\ell\ell'\mu})$ make up the final 40 fitting parameters for a monatomic system, giving us ninety-three (93) parameters in all. (Some of these, particularly the parameters with $\ell = d$ or the g - and r -parameters, may not be used for a particular calculation.)

If the basis functions which generate the overlap (20) are normalized, then in general we must have

$$|S_{\ell\ell'\mu}(R)| < 1, \quad R > 0, \quad (21)$$

and

$$S_{\ell\ell'\mu}(0) = \delta_{\ell\ell'}. \quad (22)$$

Because we have no true underlying TB basis functions, and because we determine the parameters $(p_{\ell\ell'\mu}, q_{\ell\ell'\mu}, r_{\ell\ell'\mu}, s_{\ell\ell'\mu})$ from a limited set of data, the parameters (20) do not necessarily obey the condition (21) for atomic separations which are not in our database. In particular, it is unlikely that our fitted parametric form (20) will ever obey (22). This does not

lead to problems so long as we apply these parameters to structures near those in the fitting database. However, it frequently happens that we would like to study structures outside the database, particularly those where two or more atoms are relatively close together, as occurs at an interstitial substitution. In that case, the violation of (21) can lead to unphysical behaviour of the overlap matrix, which is required to be positive definite. To help alleviate this problem, we have defined an alternate set of overlap parameters,

$$S_{\ell\ell'\mu}(R) = (\delta_{\ell\ell'} + p_{\ell\ell'\mu}R + q_{\ell\ell'\mu}R^2 + r_{\ell\ell'\mu}R^3) \exp(-s_{\ell\ell'\mu}^2 R) F(R), \quad (23)$$

which has the virtue that it satisfies (22) and does not change the parameter count. We have used overlaps of type (23) for our parametrizations of C [40], Si [21], and Ge [41]. While somewhat more satisfactory than (20), this form does not necessarily satisfy condition (21), and so may still lead to an unphysical overlap matrix. We are considering alternative methods of specifying the overlap parameters which should guarantee that the overlap matrix will always be positive definite.

As noted above, the 93 (or 97) parameters defined by (15), (17), (19), and (20) or (23) are to reproduce the contents of the first-principles database. We do this by minimizing a weighted least-squares penalty function, using the finite-difference Levenberg–Marquardt algorithm [42]. The function weights deviations from the correct total energy 100–500 times more than deviations from the correct band structure, and also can include terms which restrict the range of the exponential parameters and which penalize overlap matrices which have very small eigenvalues, a precursor to a non-physical overlap matrix.

We have computed TB parameters for the alkaline-earth, transition, and noble metals [12]; aluminium, gallium, and indium [43]; carbon [40] and silicon [21, 40]; germanium [41]; arsenic, tin, antimony, and bismuth [44]; lead [45] and magnesium [46]. The parameters are available via the Worldwide Web at <http://cst-www.nrl.navy.mil/bind/>. We will discuss the performance and transferability of these parameters in the sections below.

Methodologies similar to ours have been pursued by Xu *et al* [47] for C and Si, by Haas *et al* [48] for Mo, by Xie and Blackman [49] for Pd and Ag, and by Barreteau *et al* [50, 51] for Rh. The main difference between those works and ours is that they utilize orthogonal Hamiltonians. The first two methods also differ from ours in that they use a repulsive potential in their treatment of the total energy, rather than the shift (13) and environmentally dependent on-site parameters (17). Barreteau *et al* use our procedure with an orthogonal basis. Their results for Rh are in good agreement with ours, except that their surface energies are not well reproduced by the orthogonal Hamiltonian. In addition, Barreteau *et al* have shown that this procedure is viable in the regime of small clusters.

4.2. The tight-binding parameters—multi-component systems

The extension of the formalism of section 4.1 to multi-component systems includes both trivial and complex changes to the formalism. The hopping and overlap parameters change only slightly. For like-atom interactions (A–A, B–B, etc), we still have ten hopping and overlap parameters (18) and continue to use the parametrization forms (19) and (20) or (23). For dissimilar atoms (A–B, B–C, etc), we note that the interaction between an s orbital of atom A and a p orbital of atom B is not the same as the interaction between a p orbital of atom A and an s orbital of atom B. This means we must define an additional four SK parameters for dissimilar-atom interactions:

$$(\ell\ell'\mu) = ps\sigma, ds\sigma, dp\sigma, \text{ and } dp\pi. \quad (24)$$

We parametrize these additional hopping integrals using the form (19). For the overlap integrals, we note that although the overlap between any basis function of atom A and a basis

function of atom B must satisfy (21), it is not necessary to satisfy (22). We therefore use the parametrized form (20) for all 14 dissimilar-atom overlap integrals. Thus for an N -component system there are $28N(N - 1)$ parameters ($28 = 14 \times 4/2$) characterizing the dissimilar-atom hopping (or overlap) parameters, and $40N$ parameters characterizing the like-atom parameters.

The environmental sensitivity of the on-site terms makes for a more complicated modification. We have tried several different methods for determining the on-site parameters. Here we describe the current method, noting that it is subject to change as we gain more experience with multi-component systems.

In the following we assume that each atom i has an associated atom type \tilde{i} . Then we define the density on atom site i from atoms of type \tilde{j} to be

$$\rho_{i\tilde{j}} = \sum_j \exp(-\lambda_{\tilde{j}}^2 R_{ij}) F(R_{ij}). \quad (25)$$

There are N parameters $\lambda_{\tilde{j}}$ for an N -component system.

The on-site terms for atom i then include contributions from all atom types \tilde{j} :

$$h_{i\ell} = a_{i\ell} + \sum_{\tilde{j}} [b_{i\tilde{j}\ell} \rho_{i\tilde{j}}^{\frac{2}{3}} + c_{i\tilde{j}\ell} \rho_{i\tilde{j}}^{\frac{4}{3}} + d_{i\tilde{j}\ell} \rho_{i\tilde{j}}^2], \quad (26)$$

where the sum is over all of the atom types in the system. Since in general $b_{i\tilde{j}\ell} \neq b_{j\tilde{j}\ell}$, there will, in general, be $3N$ parameters $a_{i\ell}$, and $9N^2$ parameters $(b, c, d)_{i\tilde{j}\ell}$. Note that (25) and (26) reduce to (15) and (17) if $N = 1$.

If we add up all the parameters, we find that there are $N(28 + 65N)$ parameters to be fitted in an N -component system. Thus for a binary system we must determine 316 parameters. If we split the d on-site terms into t_{2g} and e_g components, this becomes $N(29 + 68N)$, or 330 for $N = 2$.

We have determined parameters for several sets of binary systems, including NbC, CoAl, and PdH [8, 52]. We will describe the properties of these parametrizations in the sections below.

5. Equation of state

Having determined our TB parameters we first proceed in calculating the equation of state (energy versus volume) for various structures. For the structures that we fit (fcc and bcc in the case of transition metals) the equation of state is very close (better than 1 mRyd accuracy) to that of the LAPW data. For other structures such as sc, hexagonal close packed (hcp), and diamond we usually find the correct structural energy ordering. In particular, for those non-magnetic materials that crystallize in the hcp structure we predict that hcp is the ground state, even though we included no hcp structures in our first-principles database. Our parameters for Mn even correctly describe the α -Mn structure as the ground state [53]. Similarly, the TB procedure finds other unstable or metastable structures at energies well above the ground state, consistent with independent LAPW calculations. However, for these structures the agreement between TB and LAPW is less impressive.

An illustration of one of our equation-of-state results is shown in figure 5 for titanium. The original parameters in [12] show an hcp ground state, but give a metastable hexagonal ω (*Strukturbericht* symbol C32) phase which is too high in energy. To correct this, we performed full-potential LAPW calculations in the generalized gradient approximation (GGA) [54], where we found the C32 and A3 (hcp) phases to be nearly degenerate. In our TB result the C32 phase is slightly lower in energy than the hcp phase, which is consistent with our LAPW results if not with experiment. We can ‘correct’ our TB binding parameters such that the hcp phase is

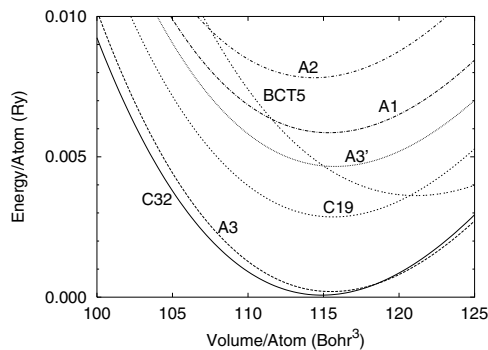


Figure 5. The NRL-TB equation of state for Ti in a variety of structures. C32 = hexagonal ω , A3 = hcp, C19 = α -Sm, A3' = α -La, A1 = fcc, A2 = bcc, BCT5 = body-centred tetragonal with fivefold coordination.

the ground state. When we do so [55], we find that these parameters predict the existence of the high-pressure orthorhombic γ -Ti phase recently observed experimentally [56].

In either case, when we look at the close-packed structures, we see that the ordering is A3 (hcp, stacking ABAB), C19 (α -Sm or ‘9R’, stacking ABCBCACAB), A3' (α -La, stacking ABACABAC), and finally A1 (fcc, stacking ABCABC). Thus the energy goes up as the stacking becomes more fcc-like, as one would expect.

We can also study crystal structures of lower symmetry. An example is the Bain path [57, 58] which occurs under a volume-conserving tetragonal strain. Figure 6(a) shows the Bain path for Cu where one notes a smooth path from the fcc ground state to the unstable bcc phase. Note that the curvature around the fcc phase is related to the elastic constant $C_{11} - C_{12}$ of Cu. We can also apply this technique to other strains. In figure 6(b) we perform a trigonal strain on gold, changing the angle between the primitive vectors. In this figure we have an fcc lattice for $\theta = 60^\circ$, a sc lattice for $\theta = 90^\circ$, and a bcc lattice for $\theta = 109.47^\circ$. The curvature around $\theta = 60^\circ$ is related to the elastic constant C_{44} of gold. Note that this figure shows that the sc phase of gold is elastically unstable.

6. Elastic constants

The procedure for calculating elastic constants from first-principles calculations is described in detail by Mehl *et al* [59, 60]. The same procedure is used in our TB calculations. Briefly, one imposes an external strain on the crystal and calculates the energy as a function of strain. For cubic materials the tetragonal shear modulus $C_{11} - C_{12}$ is found by applying a volume-conserving orthorhombic strain and the trigonal shear modulus C_{44} from a volume-conserving monoclinic strain. We summarize our results for the cubic structures in figure 7, which shows our TB and LAPW [12, 43] results together with the experimental values [61]. The C_{ij} -values for Fe and Ni are derived from a spin-polarized extension to the NRL-TB method [62] which will be discussed in section 13. The calculation of elastic constants is a very sensitive test of our method because the results depend on very small differences between the equilibrium and the distorted energies. We report results for C_{ij} at the experimental volume, as that gives results which are usually in somewhat better agreement with experiment [60]. Figure 7 shows that our TB results are in very good agreement with both the first-principles LAPW calculations and experiment. We have also generated elastic constants for the hcp materials. These results are discussed in [46, 55, 60]. Generally, the hcp elastic constant calculations are inferior to those for the cubic materials, at least when no hcp structures are included in the fitting database.

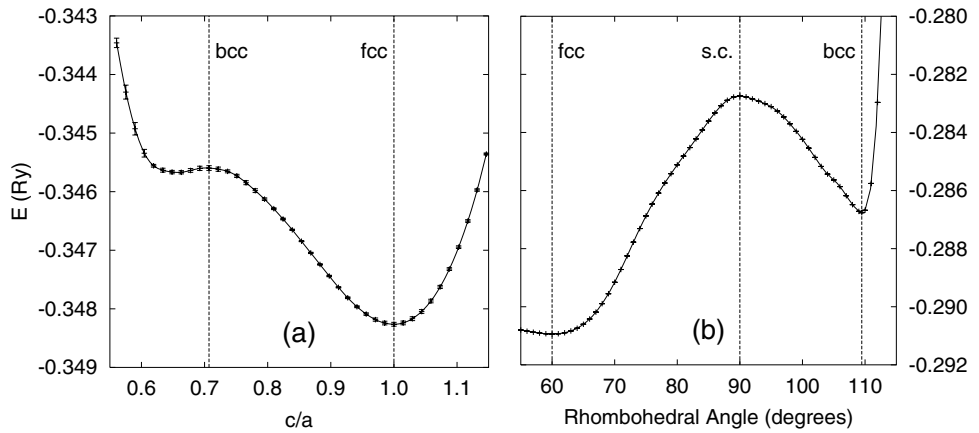


Figure 6. The NRL-TB total-energy calculations for strained unit cells, at the equilibrium experimental volume. The error bars give an estimate of the errors in the calculation due to k -point sampling. The straight lines indicate high-symmetry structures. The curves are spline fits through the data points. (a) Energy as a function of c/a in face-centred tetragonal Cu, i.e., along the Bain path. The local minimum to the left of the bcc structure is a tenfold-coordinated structure which is elastically unstable to shears in other directions. (b) Energy as a function of angle in rhombohedral Au. The bcc structure is elastically unstable to a tetragonal shear, as in (a).

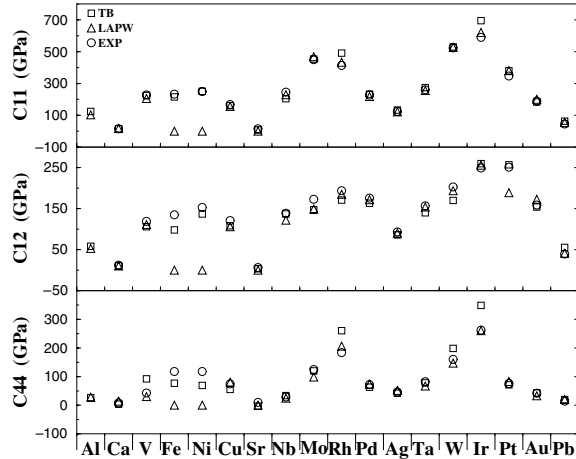


Figure 7. Elastic constants for many cubic metals, obtained from both TB and first-principles results [12, 43] and compared to experiment [61].

7. Phonon frequencies

We have determined phonon frequencies with the NRL-TB model by several methods [11, 63]. In the *frozen phonon method* [64], we create a supercell which can support a commensurate phonon mode of wavevector q . Atoms are displaced from their equilibrium positions according to a specified polarization direction and the phase of this wave at the atomic position. The dynamical matrix at q is determined from the second derivative of the total energy as a function of the amplitude of the phonon wavevector. In principle this leads to a $3N \times 3N$ matrix, but

Table 3. High-symmetry phonon frequencies of copper and gold, found by using the frozen phonon approximation [64], the NRL-TB parameters, and the full-potential LAPW method for gold. Symmetries are labelled according to the notation of Miller and Love [67, 68]. We also compare our results to experiment. All calculations were performed at the indicated experimental lattice constant, and all frequencies are in THz.

Symmetry	Polarization	Copper		Gold		
		$a = 3.61 \text{ \AA}$	Experiment [69]	NRL-TB	LAPW [63]	Experiment [70]
X ₃	Longitudinal	7.25	7.27	5.29	4.43	4.60
X ₅	Transverse	5.13	4.74	2.87		2.72
L ₂	Longitudinal	7.93	7.30	5.35	4.53	4.69
L ₅	Transverse	3.47	3.42	1.91		1.85
W ₂	Longitudinal	4.75	4.95	2.66		2.63
W ₅	Transverse	5.70	6.10	4.01		3.62

application of symmetry [65]² will reduce the size of the matrix at highly symmetric points in the Brillouin zone. We did not consider anharmonic contributions to the phonon frequency [66], but this is a simple addition to the method.

Table 3 shows the phonon frequencies of copper and gold at several high-symmetry points in the fcc Brillouin zone, labelled using the notation of Miller and Love [67, 68]. We compare to LAPW results for gold [63] and to experiment [69, 70]. For this calculation we used the gold parameters described in [63], and calculated copper parameters using the same method³. Most frequencies are found to be within 10% of the experimental value, and the RMS error over all these points is 0.6 THz. If more accurate phonon frequencies are required, one can expand the first-principles database described in [63] to include first-principles LAPW frozen phonon calculations.

The frozen phonon method can also be applied to multi-atom unit cells. There are several different modes at each wavevector, so we use the program FROZSL to determine the appropriate supercell for each mode. In table 4 we show NRL-TB results for the phonon spectra of diamond structure C and Si [21] compared to experiment [71, 72], using the TB parameters of [40]. (See section 11 for more details about these parametrizations.) The largest disagreement between theory and experiment is 5.5 THz, and the RMS error is 1.8 THz.

The tight-binding molecular dynamics (TBMD) code, written by Kirchhoff⁴, can compute forces in supercells. This allows us to directly calculate the real-space dynamical matrix by moving one atom in a large supercell, calculating the forces on the other atoms in the supercell, and differentiating to calculate the dynamical matrix. This matrix can then be Fourier transformed to calculate the phonon frequencies at wavevector q [73]. This can be applied to calculations at arbitrary q if the supercell is large enough that the forces vanish for atoms far from the displaced atom. We have previously shown the results of this calculation for gold [63]. Here we present similar results for copper in figure 8.

Finally, we can determine the phonon spectrum at finite temperature from a molecular dynamics (MD) calculation by calculating the velocity–velocity autocorrelation function and performing a Fourier transform. This technique is discussed in [63] and section 12.

² We use the program FROZSL (<http://128.187.202.55/~stokes/frozsl.html>) to determine phonon frequencies for complex crystals. For simple unit cells, see <http://cst-www.nrl.navy.mil/~mehl/phonons/>

³ The NRL-TB parameters used in this study for copper and gold are available at http://cst-www.nrl.navy.mil/bind/cu_par_99 and http://cst-www.nrl.navy.mil/bind/au_par_99, respectively.

⁴ For a complete description of the TBMD program, see <http://cst-www.nrl.navy.mil/~kirch/tbmd/>

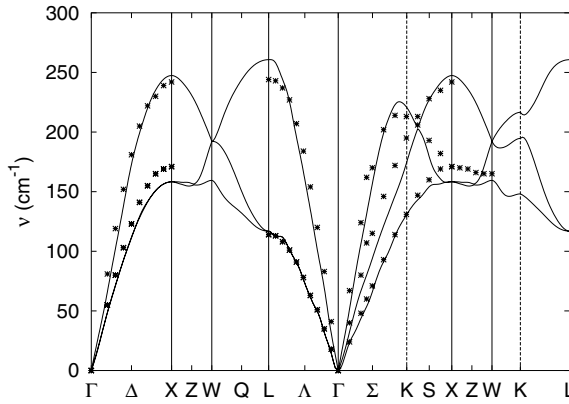


Figure 8. Phonon frequencies of copper, at the experimental lattice constant, computed by Fourier transformation and diagonalization of the real-space dynamical matrix [63]. The points are from experiment [69].

Table 4. Phonon frequencies of diamond structure C and Si, calculated using the frozen phonon approximation and the NRL-TB parameters [40] and compared to experiment. Symmetries are labelled according to the notation of Miller and Love [67, 68]. Under the column labelled polarization, ‘L’ is longitudinal, ‘T’ is transverse, ‘A’ is acoustic, and ‘O’ is optical. Thus ‘TO’ is a transverse optical mode. All frequencies are given in THz.

Symmetry	Polarization	Carbon $a = 3.567 \text{ \AA}$		Silicon $a = 5.430 \text{ \AA}$	
		NRL-TB	Experiment [71]	NRL-TB	Experiment [72]
Γ'_{25}		39.3	39.9	15.9	15.5
X_1	LA	34.2	35.5	12.1	12.3
X_3	TO	29.8	32.1	15.2	13.9
X_4	TA	24.7	24.2	4.8	4.5
L_1	LO	39.3	36.6	16.7	
L'_2	LA	36.5	31.0	10.0	
L_{3+}	TA	17.6	16.9	3.8	3.4
L_{3-}	TO	35.3	36.2	16.0	14.7
W_1		28.7	30	11.1	12.1
W_2		33.3	35	15.4	14.7
		27.9	28	6.4	4.2

8. Vacancies

To calculate vacancy formation energies we have used a supercell approach [74, 75]. One atom in the supercell is removed and neighbouring atoms are allowed to relax around this vacancy while preserving the symmetry of the lattice. We eliminate the vacancy–vacancy interaction by using a large supercell. We found that a unit cell with 128 atoms was large enough to eliminate vacancy–vacancy interactions. This size cell is computationally trivial for our TB scheme, but prohibitively slow with first-principles methods such as LAPW.

The vacancy formation energy for an N -atom supercell is given by the expression

$$E_{vf}(N) = E(N-1, 1) - \frac{N-1}{N} E(N, 0), \quad (27)$$

where $E(N, M)$ is the energy of an $(N+M)$ -site supercell containing N atoms and M vacancies.

Table 5. Vacancy formation energy (in eV) for selected elements obtained using the NRL-TB method, along with comparisons to experiment, where available. All calculations are performed in 128-atom supercells fixed at the experimental volume, with internal relaxation. Unless otherwise noted, calculated results are from [12] and experimental results from [76].

Element	TB result	First principles	Experiment
Al	0.40 [43]	0.56 [74], 0.84 [75]	0.66 [77]
Cu	1.18	1.41 [79], 1.29 [80]	1.28–1.42
Nb	2.82		2.65 ± 0.03
Mo	2.46		3.0–3.6
Rh	3.35	2.26 [80]	1.71 [78]
Pd	2.45	1.57 [79]	1.85 ± 0.25
Ag	1.24	1.20 [79], 1.06 [80]	1.11–1.31
Ta	2.95		2.9 ± 0.4
W	6.43		4.6 ± 0.8
Ir	2.17		1.97 [78]
Pt	2.79		1.35 ± 0.09
Au	1.12		0.89 ± 0.04

Thus

$$E(N, 0) = NE_{\text{bulk}} \quad (28)$$

where E_{bulk} is the energy of one atom in the bulk material. A selection of our vacancy formation results is shown in table 5, where we compare to both experimental [76–78] and first-principles [74, 75, 79, 80] values. It is clear that the effect of relaxation is small. Comparing to experiment we note that we reproduced the trend that the noble metals have vacancy formation energies of about 1 eV while the bcc transition metals have much larger values. Quantitative agreement between TB results and experiment is unlikely, partly due to large deviations between different experiments.

The calculation of vacancy formation energies presents us with an opportunity to demonstrate the efficiency of the TB method. Figure 9 shows the time needed to calculate the formation energy of copper as a function of supercell size, using both the full-potential LAPW method and our TB method. We see that the TB method is approximately 1000 times faster than the LAPW calculation for all unit-cell sizes.

9. Surfaces

Chadi [83, 84] pioneered work on semiconductor surfaces, applying total-energy minimization to the determination of the atomic geometries of the (110) surface of Si, Ge, GaAs, and other compound semiconductors. He also studied aspects of the structure and energetics of high-Miller-index Si surfaces, obtaining interesting results for the ideal and reconstructed vicinal surfaces. The NRL-TB scheme was also applied to Si [21], giving high-quality results for energetics of the low-index Si surfaces.

We calculate the energy needed to form a clean surface by applying a supercell technique: cleave the crystal along a plane, creating two identical free surfaces. Repeat this periodically in the direction perpendicular to the surfaces. We separate the slabs by a large region of vacuum, greater than the TB cut-off distance R_c (see (16)), which prohibits electrons from hopping between slabs. We make the slabs thick enough that in the centre of the slab we have the properties of the bulk material and the two surfaces of the slab do not interact with each other. This is easy to do within a TB simulation, and much more difficult in a first-principles calculation. Using the above requirements we find that for non-magnetic fcc and bcc metals a

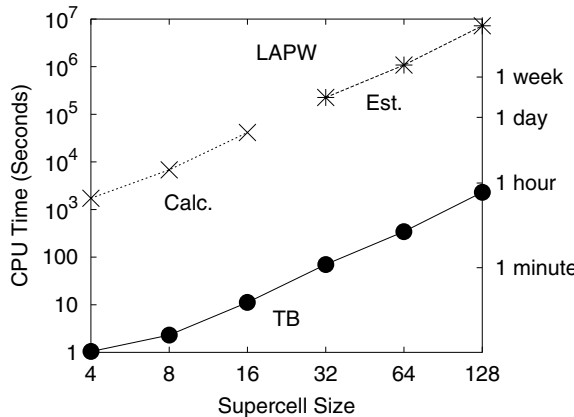


Figure 9. Computational time needed to calculate the vacancy formation energy of copper as a function of supercell size. The bottom line shows the time needed by the NRL-TB method. The top line shows the time needed for a self-consistent LAPW calculation. The LAPW results were only computed for cells up to 16 atoms. The line from 32-atom cells up is an estimate assuming N^3 -scaling. These calculations were done using a single 200 MHz processor. Modern systems will reduce the time, but should maintain the ratio between TB and LAPW results.

slab of 25 atomic layers is sufficient. To ensure convergence with respect to k -points we used up to 91 k -points in the two-dimensional Brillouin zone. The surface energy is defined as the energy required to create a unit area of new surface and is given by the expression

$$\gamma_s = \frac{1}{2A}(E_{\text{slab}} - NE_{\text{bulk}}) \quad (29)$$

where A is the area occupied by one unit cell on the surface of the slab, E_{slab} is the total energy of the slab, N is the number of atoms in the unit cell, and E_{bulk} is the energy of one atom in the bulk. These calculations were done at the equilibrium lattice parameter without relaxation or reconstruction at the surface. Our results are shown in figure 10. For comparison with experiment we use an ‘average’ face extrapolated to $T = 0$ K. Our results are in good agreement with experiment [81, 82], unlike the EAM [85, 86] results which are significantly lower than experimental ones. For the fcc metals we find that the close-packed surfaces are the most stable, i.e.,

$$\gamma_s(111) < \gamma_s(110) < \gamma_s(100). \quad (30)$$

For the bcc metals,

$$\gamma_s(110) < \gamma_s(100) < \gamma_s(111). \quad (31)$$

10. Stacking faults and ductility

The stability of stacking faults on slip planes of a crystal is directly connected to the mobility of dislocations on those planes. As discussed by Rice and co-workers [87–89], the ductility of a metal is at least partially determined by the competition between dislocation motion and the energy needed to form a new crystalline surface, γ_s (29). In a close-packed crystal, a stacking fault is produced by the translation of one surface of a crystal across the face of the other surface. In an fcc crystal, we consider the lowest-energy (111) surface (30). Then a typical stacking fault is along the $\langle 121 \rangle$ direction. A stable stacking fault results when the displacement reaches

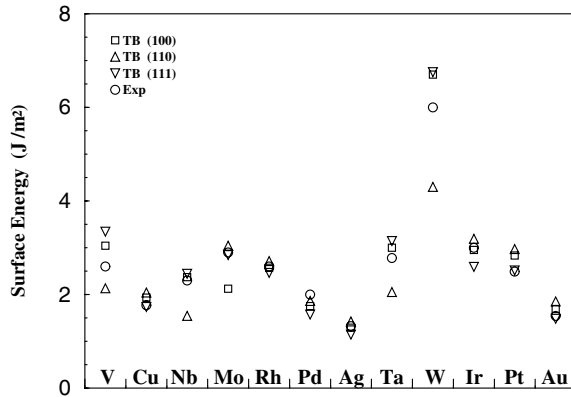


Figure 10. Low-index surface energies of several transition and noble metals, calculated within the NRL-TB method. Experimental values are for an ‘average’ surface extrapolated to $T = 0$ K [81, 82].

Table 6. Intrinsic stacking fault energy γ_{is} , surface energy γ_s , unstable stacking fault energy γ_{us} , and Rice ductility parameter D (32) for the fcc metals, obtained from the NRL-TB method. Energies are expressed in mJ m^{-2} .

Element	γ_{is} [90]	γ_s [12, 43]	γ_{us} [90]	D (equation (32))
Al	96	870	176	1.50
Cu	18	1730	162	3.24
Rh	344	2460	714	1.04
Pd	166	1570	439	1.08
Ag	29	1140	108	3.20
Ir	569	2590	902	0.87
Pt	373	2510	497	1.53
Au	50	1480	129	3.48
Pb	58	888	166	1.59

a value of $a/\sqrt{6}$, where a is the fcc lattice constant. The stacking in the $\langle 111 \rangle$ direction at that point looks like $\cdots \text{ABCABC|BCABCA} \cdots$, where the ‘|’ represents the stacking fault. In this region the stacking is hcp-like (BCBC) rather than fcc-like (ABCABC). The energy associated with the stacking fault is just the energy difference per unit area of interface between this system and the perfect crystal, and is denoted as γ_{is} , the intrinsic stacking fault energy.

Since the perfect fcc crystal is the lowest energy of the solid, and the intrinsic stacking fault is metastable, it follows that there must be some maximum energy achieved as we move the stacking fault along the $\langle 112 \rangle$ direction. This maximum is denoted as γ_{us} , the unstable stacking fault energy. Rice [88] has shown that we can use the γ_{us} and the surface energy γ_s to construct a ‘ductility parameter’,

$$D = 0.3 \frac{\gamma_s}{\gamma_{us}}. \quad (32)$$

When $D > 1$, systems tend to be ductile.

We have used (32) and the NRL-TB method to study the ductility of the fcc metals [90]. Table 6 shows the calculated values of γ_s , γ_{us} , D , and, for completeness, γ_{is} for the fcc metals, obtained using the NRL-TB parameters. Note that the obviously ductile metals (gold, silver, lead) have relatively large values of D . The less ductile metals (Ir, Rh, Pd) have smaller values.

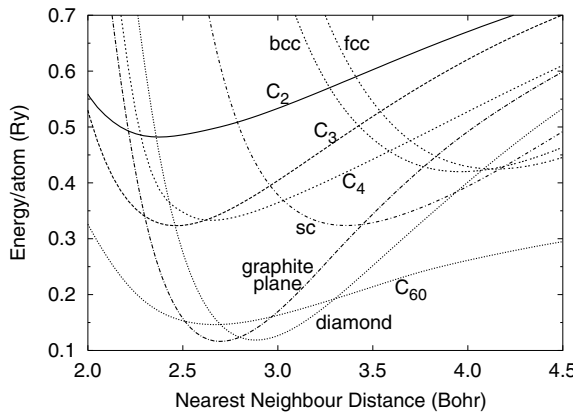


Figure 11. Energy of various carbon structures as a function of nearest-neighbour separation. Curves labelled C_2 , C_3 , C_4 , and C_{60} represent the corresponding isolated molecules.

11. Semiconductors

The NRL-TB method has also been applied to semiconductors such as C [40], Si [21, 40], and Ge [41]. Our carbon parameters include only the four sp orbitals on each atom. For Si and Ge we generated two sets of parameters: one with only sp orbitals, and one with s, p, and d orbitals. The four sp parameters ($ss\sigma$, $sp\sigma$, $pp\sigma$, and $pp\pi$) satisfy the sign convention of Harrison [7]. The fitting procedure for semiconductors deviates from the procedure we used for most metals. For most of the transition and noble metals we were able to get good TB parameters by fitting to only the bcc and fcc structures. For carbon we also included fits to the sc, diamond, and graphite structures, as well as the C_2 dimer. In figure 11 we show our results for the total energy of carbon as a function of the nearest-neighbour distance in several structures, including molecules that were not fitted. The energy difference between the diamond and graphite structures is nearly zero, consistent with our LAPW results. It is particularly noteworthy that the energetics and structure of C_{60} , which was not fitted, is in very good agreement with independent first-principles calculations. In addition, our calculated band structure of an fcc C_{60} crystal is in very good agreement with first-principles calculations [91].

We have also done an extensive TB study of Si [21], for which we fitted the fcc, bcc, sc, and diamond structures. We obtained equations of state for many other structures, including the high-pressure β -Sn phase and the low-density clathrate phase, which were found to be in good agreement with first-principles results. In [21] we present details of our Si study that demonstrate that our approach is accurate for the calculation of surface and interstitial energies, as well as phonon spectra. In table 7 we compare the TB, LAPW, and experimental elastic constants of C, Si, and Ge. We have also computed phonon frequencies for C and Si, as was shown in table 4. Our methodology has also been applied to other covalently bonded materials such as tin [44].

12. Molecular dynamics

The NRL-TB method has been extended to the regime of MD simulations by Kirchhoff, who built a parallel MD code. This code uses the environment- and bond-length-dependent parameters described in section 4 and calculates the electronic structure, total energy, and atomic forces, using either direct diagonalization or the kernel polynomial method (KPM) [92]. In the applications we have performed so far our systems contain supercells of 343 atoms, which are derived by replicating a primitive fcc unit cell seven times along each of the primitive lattice

Table 7. Elastic constants (in GPa) of diamond structure C [40], Si [21], and Ge [41], as determined by our TB method, first-principles LAPW calculations, and experiment. All calculations were done at the room temperature equilibrium volume. The calculations labelled C_{44} (ub) were done by keeping the carbon atoms at fixed lattice coordinates as we strained the lattice.

	Carbon			Silicon			Germanium	
	TB	LAPW	Experiment	TB	LAPW	Experiment	TB	Experiment
C_{11}	1036	1037	1076	179	152	166	144	129
C_{12}	48	111	125	73	60	64	28	48
C_{44} (ub)	601	555		135	101		138	
C_{44}	601		576	95		80	112	67

directions. For such systems, direct diagonalization is faster than the order- N^2 KPM method. We only sample the Γ point of the supercell Brillouin zone. This approximation, which speeds the program considerably, is certainly very good for non-metals, but we find that even for metals it is accurate to within 10%. The MD simulations are started with atoms placed on the regular lattice and with random velocities found from a Boltzmann distribution function for a temperature of $2T$. The calculations are performed in a micro-canonical ensemble guaranteeing an equilibrium temperature T . The usual Verlet algorithm is used to integrate the equations of motion. We have previously presented results for Si [21] and Au [63]. In these papers we calculated the phonon dispersion curves and densities of states as a function of temperature by applying a Fourier transform of the velocity–velocity autocorrelation function. We also calculated the temperature dependence of the lattice parameter, from which we extracted the thermal expansion coefficient. Finally, using the atomic positions generated by the MD simulations at several temperatures we computed an atomic mean square displacement in very good agreement with experiment.

13. Magnetism

In our earlier work [10] we applied the SK method to the ferromagnetic metals Co, Fe, and Ni. In these calculations we determined the parameters by fitting separately to the spin-up and spin-down APW energy bands, thus obtaining two different sets of parameters which are coupled in the determination of the Fermi level. These early calculations give an accurate account of the band structure of these metals but do not provide total-energy information. One of the virtues of the SK scheme is that it is convenient to use it for empirical adjustments of the band structure to better account for discrepancies comparing to experiment. We have applied such an adjustment of the d-band exchange splitting for Ni to match photoemission measurements and on that basis to calculate the Curie temperature [93] using a Stoner model procedure.

In our latest work we have extended the NRL-TB method to describe spin-polarized systems. For Fe it is known [94] that the local density approximation (LDA) does not yield the correct ground state, so our LAPW fitting database consists of results using the GGA exchange–correlation functional [54], which provides the correct total-energy ordering of structures. An important ingredient of these calculations is that we choose the hopping and overlap parameters independent of the spin, so the exchange splitting enters via the on-site parameters, which differ between the two spins. Our procedure is to simultaneously fit bands and total energies for three crystal structures, e.g., paramagnetic and ferromagnetic bcc, and paramagnetic fcc. We then use the resulting Hamiltonian to calculate the total energy and other properties for various crystal structures. Comparisons with independent LAPW results for the structures in the fit

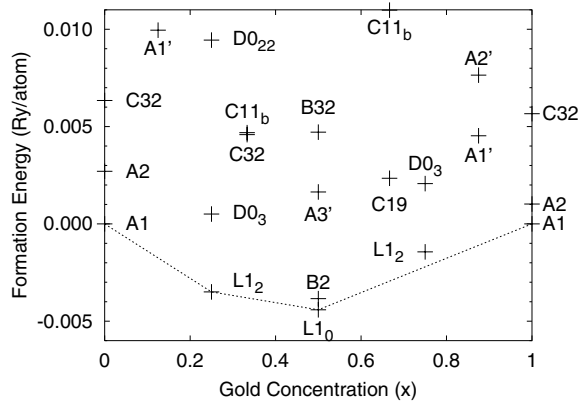


Figure 12. The NRL-TB formation energy for a variety of structures in the $\text{Cu}_{1-x}\text{Au}_x$ system. Most structures are identified by their *Strukturbericht* symbols. The symbol $\text{A}1'$ denotes the Ca_7Ge structure [99], an eight-atom supercell of the fcc lattice. The structure $\text{A}2'$ is a similar supercell of the bcc lattice. Only structures which touch the tie-line are stable; the others will spontaneously phase separate into stable structures.

are excellent for Fe [62] and Ni (which will be presented in a later publication). We have also used this TB parametrization for Fe as the starting point for implementing Pickett's theory [95] for non-collinear magnetism [96]. Finally, we wish to mention that the TB approach is also a convenient formalism for incorporating spin-orbit coupling, as we have shown in a recent paper describing the band structure of semiconductors [97].

14. Binary compounds

As noted in section 4.2, we have begun to apply our tight-binding methodology to two-component systems, including NbC, CoAl, and PdH [8, 52]. In this section, we will briefly describe the creation and use of a set of TB parameters for the Cu–Au system. This will serve to illustrate the care needed to construct good parameters for binary compounds. Note that we originally picked this system because it seemed rather simple, and because it is well described by atomistic potentials such as the SMA [38].

Since we do not want to lose our excellent parametrizations for Cu and Au, we will freeze these parameters in the combined Cu–Au fit. Thus the only parameters to be fitted are those which couple interactions between different kinds of atom. This includes the on-site parameter cross-terms (26) as well as the parameters making up the new SK and overlap integrals. In all, there are 130 parameters which must be determined in our scheme.

The phase diagram for the Cu–Au system [98] shows that there are only five possible ordered phases: pure Cu (fcc), Cu_3Au in the $\text{L}1_2$ structure, CuAu in the $\text{L}1_0$ structure, CuAu_3 in the $\text{L}1_2$ structure, and pure Au (fcc). We therefore began construction of our first-principles database by using the $\text{L}1_2$ phases of Cu_3Au and CuAu_3 , and the $\text{L}1_0$ phase of CuAu . The latter phase is tetragonal, so we must include changes in both volume and c/a in the database.

Our work on elemental systems [12] showed us that it is important to include some structures other than the ground state in the database. We therefore included the bcc-like $\text{D}0_3$ phase of both Cu_3Au and CuAu_3 in the fit, as well as the NaCl (B1) and CsCl (B2) phases of CuAu . These are all cubic phases with no relaxation, so the first-principles calculations were rather simple⁵.

⁵ In this article we characterize crystals by their *Strukturbericht* symbols. All of the structures used in this paper are fully described at <http://cst-www.nrl.navy.mil/lattice/>

Experimentally, and in our LAPW calculations, the ground state of the 50–50 alloy is the L₁₀ phase. This phase can be constructed by taking an fcc unit cell of copper, and replacing alternate [001] planes of copper atoms by gold. The Cu–Au parameters constructed from the database did not show this to be the ground state, however. Instead, we found that the L₁₁ structure was the ground state. This structure can also be constructed from a fcc crystal, with alternating [111] planes of Cu and Au. We did first-principles calculations for the L₁₁ phase, and found that it is indeed above the L₁₀ phase. We then added these calculations to the database, and refitted the Cu–Au parameters. The new parameters showed that the L₁₀ phase is lower in energy than the L₁₁ phase, and is lower in energy than any of the other 50–50 structures that we tried.

We tested our parameters over a wide range of structures in the Cu_{1-x}Au_x system. In figure 12 we express our results in terms of the formation energy of this compound. This is defined as the energy per atom needed to combine Cu and Au into an alloy structure. Formation energies of stable phases are negative; that is, combining Cu and Au into, say, L₁₀ CuAu is favoured and so will give off a certain amount of heat. To reduce clutter we have not included all of our calculations in this figure. We do show the lowest-energy structure that we have found at each concentration, as well as some of the higher-energy structures.

The tie-line drawn on figure 12 connects the stable structures of the Cu–Au system. Structures with energies above this line will spontaneously phase separate into stable structures. Thus the A1' (properly, Ca₇Ge [99]) structure of Cu₇Au ($x = 1/8$) will spontaneously decomposed into fcc Cu and L₁₂ Cu₃Au, in agreement with the published phase diagram. We note that the L₁₂ phase of CuAu₃ is slightly above the tie-line, which agrees with neither the published phase diagram [98] nor our LAPW calculations. This indicates that we will have to do some more fitting to correctly describe the Au-rich phases in this system. This work is under way, along with work to find a complete description of the elastic constants and phonon modes of the Cu–Au system. Results for the Cu₃Au L₁₂ structure, including elastic constants, phonon frequencies and the electronic structure of the (111) surface are given in Lekka *et al* [100].

We conclude this section by summarizing our application of the NRL-TB method to the Pd–H system [52]. In this application we fitted first-principles results for potential energy surfaces for the dissociation of hydrogen molecules on palladium. The description of reactions at surfaces requires a search of a configuration space which exceeds 12 dimensions. Therefore the NRL-TB scheme, which was used to interpolate a small number of *ab initio* energies, is an efficient procedure for addressing this problem. We used a 10 × 10 Hamiltonian per molecule, constructed from our pure non-orthogonal spd Pd parameters⁶, with the addition of new s-orbital hydrogen and H–Pd parameters, which were determined by fitting to the *ab initio* energies for Pd–H surfaces. We reproduced the first-principles potential energy surface with an RMS error of 0.1 eV, demonstrating the applicability of this approach to the problem of dissociation of molecules at surfaces. The obvious next step is to perform a MD simulation involving many atoms and trajectories.

Acknowledgments

We wish to thank our collaborators in these projects, including B Akdim, N C Bacalis, M Z Bazant, N Bernstein, R E Cohen, S C Erwin, G A Evangelakis, H Gotsis, A Gross, M Herbranson, C Lekka, G C Kallinteris, E Kaxiras, M Keegan, F S Khan, N Kioussis, F Kirchhoff, M Lach-hab, I I Mazin, N I Papanicolaou, M R Pederson, W E Pickett,

⁶ We used our long-range ($R_c = 10.5$ bohr) Pd parameters, available at http://cst-www.nrl.navy.mil/bind/pd_par.

M Scheffler, D J Singh, and S H Yang. The authors were supported by the US Office of Naval Research. Development of the NRL-TB codes was partially supported by the US Department of Defense Common HPC Software Support Initiative (CHSSI). Some computational support was provided by the US High Performance Computing Modernization Program, at the Aeronautical Systems Center, Wright-Patterson Air Force Base, Dayton, OH; the Army Research Laboratory, Aberdeen, MD; and the Maui High Performance Computing Center, Kihei, HI.

References

- [1] Slater J C and Koster G F 1954 *Phys. Rev.* **94** 1498
- [2] Nussbaum A 1966 *Solid State Phys.* **18** 165
- [3] Heine V 1980 *Solid State Phys.* **35** 1
- [4] Bullett D W 1980 *Solid State Phys.* **35** 129
- [5] Haydock R 1980 *Solid State Phys.* **35** 216
- [6] Kelly M J 1980 *Solid State Phys.* **35** 296
- [7] Harrison W A 1980 *Electronic Structure and the Properties of Solids* (San Francisco, CA: Freeman)
- [8] Mehl M J and Papaconstantopoulos D A 1998 *Topics in Computational Materials Science* ed C Y Fong (Singapore: World Scientific) ch 5
- [9] Horsfield A P and Bratkovsky A M 2000 *J. Phys.: Condens. Matter* **12** R1
- [10] Papaconstantopoulos D A 1986 *Handbook of Electronic Structure of Elemental Solids* (New York: Plenum)
- [11] Cohen R E, Mehl M J and Papaconstantopoulos D A 1994 *Phys. Rev. B* **50** 14694
- [12] Mehl M J and Papaconstantopoulos D A 1996 *Phys. Rev. B* **54** 4519
- [13] Bloch F 1928 *Z. Phys.* **52** 555
- [14] Löwdin P O 1950 *J. Chem. Phys.* **18** 365
- [15] Hohenberg P and Kohn W 1964 *Phys. Rev.* **136** B864
- [16] Kohn W and Sham L J 1965 *Phys. Rev.* **140** A1133
- [17] Mercer J L Jr and Chou M Y 1994 *Phys. Rev. B* **49** 8506
- [18] Cohen R E, Stixrude L and Wasserman E 1997 *Phys. Rev. B* **56** 8575
- [19] Mattheiss L F 1972 *Phys. Rev. B* **5** 290
- [20] Laufer P M and Papaconstantopoulos D A 1986 *Phys. Rev. B* **33** 5135
- [21] Bernstein N, Mehl M J, Papaconstantopoulos D A, Papanicolaou N I, Bazant M Z and Kaxiras E 2000 *Phys. Rev. B* **62** 4477
- [22] Shore J D and Papaconstantopoulos D A 1984 *J. Phys. Chem. Solids* **45** 439
- [23] Sigalas M, Papaconstantopoulos D A and Bacalis N C 1992 *Phys. Rev. B* **45** 5777
- [24] Sigalas M M and Papaconstantopoulos D A 1994 *Phys. Rev. B* **50** 7255
- [25] Papaconstantopoulos D A, Klein B M, Faulkner J S and Boyer L L 1978 *Phys. Rev. B* **18** 2784
- [26] Papaconstantopoulos D A and Laufer P M 1987 *J. Less Common Met.* **130** 229
- [27] Julien J P, Papaconstantopoulos D A, Singh D J, Pickett W E and Cyrot-Lackmann F 1994 *Physica C* **220** 359
- [28] Papaconstantopoulos D A and Pickett W E 1998 *Phys. Rev. B* **57** 12751
- [29] Mazin I I, Papaconstantopoulos D A and Singh D J 2000 *Phys. Rev. B* **61** 5233
- [30] Andersen O K 1975 *Phys. Rev. B* **12** 3060
- [31] Wei S H and Krakauer H 1985 *Phys. Rev. Lett.* **55** 1200
- [32] DeWeert M J, Papaconstantopoulos D A and Pickett W E 1989 *Phys. Rev. B* **39** 4235
- [33] Papaconstantopoulos D A, Pickett W E and DeWeert M J 1988 *Phys. Rev. Lett.* **61** 211
- [34] Daw M S and Baskes M I 1983 *Phys. Rev. Lett.* **50** 1285
- [35] Voter A F 1994 *Intermetallic Compounds: Principles and Applications* vol 1, ed J H Westbrook and R L Fleischer (London: Wiley) ch 4
- [36] Sigalas M M and Papaconstantopoulos D A 1994 *Phys. Rev. B* **49** 1574
- [37] Kallinteris G C, Papanicolaou M I, Evangelakis G A and Papaconstantopoulos D A 1997 *Phys. Rev. B* **55** 2150
- [38] Papanicolaou N I, Kallinteris G C, Evangelakis G A, Papaconstantopoulos D A and Mehl M J 1998 *J. Phys.: Condens. Matter* **10** 10979
- [39] McMahan A K and Klepeis J E 1997 *Phys. Rev. B* **56** 12250
- [40] Papaconstantopoulos D A, Mehl M J, Erwin S C and Pederson M R 1998 *Tight-Binding Approach to Computational Materials Science (MRS Proc. vol 491)* ed P E A Turchi, A Gonis and L Columbo (Warrendale, PA: Materials Research Society) p 221

- [41] Bernstein N, Mehl M J and Papaconstantopoulos D A 2002 *Phys. Rev. B* **66** 075212
[42] More J J 1997 *Numerical Analysis* ed G A Watson (Berlin: Springer)
[43] Yang S H, Mehl M J and Papaconstantopoulos D A 1998 *Phys. Rev. B* **57** R2013 (rapid communications)
[44] Akdim B, Papaconstantopoulos D A and Mehl M J 2002 *Phil. Mag. B* **82** 47
[45] Papaconstantopoulos D A, Mehl M J and Akdim B 1998 *Proc. Int. Symp. on Novel Materials (Bhubaneswar, India, March 1997)* ed B K Rao p 393
[46] Gotsis H J, Papaconstantopoulos D A and Mehl M J 2002 *Phys. Rev. B* **65** 134101
[47] Xu C H, Wang C Z, Chan C T and Ho K M 1992 *J. Phys.: Condens. Matter* **4** 6047
[48] Haas H, Wang C Z, Fahnle M, Elsasser C and Ho K M 1998 *Phys. Rev. B* **57** 1461
[49] Xie Y and Blackman J A 2001 *Phys. Rev. B* **64** 195115
[50] Barreteau C, Spanjaard D and Desjonquères M C 1998 *Phys. Rev. B* **58** 9721
[51] Barreteau C, Guirado-López R, Spanjaard D, Desjonquères M C and Oleś A M 2000 *Phys. Rev. B* **61** 7781
[52] Gross A, Scheffler M, Mehl M J and Papaconstantopoulos D A 1999 *Phys. Rev. Lett.* **82** 1209
[53] Mehl M J and Papaconstantopoulos D A 1995 *Europhys. Lett.* **31** 537
[54] Perdew J P 1991 *Electronic Structure of Solids '91* ed P Ziesche and H Eschrig (Berlin: Akademie) p 11
[55] Mehl M J and Papaconstantopoulos D A 2002 *Europhys. Lett.* **60** 248
[56] Vohra Y K and Spencer P T 2001 *Phys. Rev. Lett.* **86** 3068
[57] Bain E C 1924 *Trans. Am. Inst. Mineral. Metall. Eng.* **70** 25
[58] Alippil P, Marcus P M and Scheffler M 1997 *Phys. Rev. Lett.* **78** 3892
[59] Mehl M J 1993 *Phys. Rev. B* **47** 2493
[60] Mehl M J, Klein B M and Papaconstantopoulos D A 1994 *Intermetallic Compounds: Principles and Practice* vol 1, ed J H Westbrook and R L Fleischer (London: Wiley) ch 9
[61] Simmons G and Wang H 1971 *Single Crystal Elastic Constants and Calculated Aggregate Properties: a Handbook* 2nd edn (Cambridge, MA: MIT Press)
[62] Bacalis N C, Papaconstantopoulos D A, Mehl M J and Lach-hab M 2001 *Physica B* **296** 125
[63] Kirchhoff F, Mehl M J, Papanicolaou N I, Papaconstantopoulos D A and Khan F S 2001 *Phys. Rev. B* **63** 195101
[64] Wei S W and Chou M Y 1992 *Phys. Rev. Lett.* **69** 2799
[65] Stokes H T 1995 *Ferroelectrics* **164** 183
[66] Klein B M and Cohen R E 1992 *Phys. Rev. B* **45** 12405
[67] Miller S C and Love W F 1967 *Tables of Irreducible Representations of Space Groups and Co-Representations of Magnetic Space Groups* (Boulder, CO: Prueett)
[68] Stokes H T and Hatch D M 1988 *Isotropy Subgroups of the 230 Crystallographic Space Groups* (Singapore: World Scientific)
[69] Nicklow R M, Gilat G, Smith H G, Raubenheimer L J and Wilkinson M K 1967 *Phys. Rev.* **164** 922
[70] Lynn J W, Smith H G and Nicklow R M 1973 *Phys. Rev. B* **8** 3493
[71] Warren J L, Yarnell J L, Dolling G and Crowley R A 1967 *Phys. Rev.* **158** 805
[72] Wei S and Chou M Y 1994 *Phys. Rev. B* **50** 2221
[73] Ackland G J, Warren M C and Clark S J 1997 *J. Phys.: Condens. Matter* **9** 7861
[74] Gillan M J 1989 *J. Phys.: Condens. Matter* **1** 689
[75] Mehl M J and Klein B M 1991 *Physica B* **172** 211
[76] Schaefer H E 1987 *Phys. Status Solidi a* **102** 47
[77] Fluss M J, Smedskjaer L C, Chason M K, Legnini D G and Siegel R W 1978 *Phys. Rev. B* **17** 3444
[78] de Boer F R, Boom R, Mattens W C M, Miedema A R and Niessen A K 1988 *Cohesion in Metals* vol 1 (Amsterdam: North-Holland)
[79] Dederichs P H, Hoshino T, Drittler B, Abraham K and Zeller R 1991 *Physica B* **172** 203
[80] Polatoglou H M, Methfessel M and Scheffler M 1993 *Phys. Rev. B* **48** 1877
[81] Baskes M I 1992 *Phys. Rev. B* **46** 2727
[82] Tyson W R and Miller W A 1997 *Surf. Sci.* **62** 267
[83] Chadi D J 1979 *Phys. Rev. B* **19** 2074
[84] Chadi D J 1984 *Phys. Rev. B* **29** 785
[85] Foiles S M, Baskes M I and Daw M S 1986 *Phys. Rev. B* **33** 7983
[86] Guellil A M and Adams J B 1992 *J. Mater. Res.* **7** 639
[87] Rice J R and Thomson R M 1974 *Phil. Mag.* **29** 73
[88] Rice J R 1992 *J. Mech. Phys. Solids* **40** 239
[89] Rice J R and Beltz G E 1994 *J. Mech. Phys. Solids* **42** 333
[90] Mehl M J, Papaconstantopoulos D A, Kioussis N and Herbranson M 2000 *Phys. Rev. B* **61** 4894
[91] Erwin S C and Pickett W E 1991 *Science* **254** 842

- [92] Silver R N, Roeder H, Voter A F and Kress J D 1996 *J. Comput. Phys.* **124** 115
- [93] Bacalis N C, Theodorakopoulis N and Papaconstantopoulos D A 1997 *Phys. Rev. B* **55** 11391
- [94] Wang C S, Klein B M and Krakauer H 1985 *Phys. Rev. Lett.* **54** 1852
- [95] Pickett W E 1996 *J. Korean Phys. Soc.* **29** 570
- [96] Mehl M J, Papaconstantopoulos D A, Mazin I I, Bacalis N C and Pickett W E 2001 *J. Appl. Phys.* **89** 6880
- [97] Lach-hab M, Papaconstantopoulos D A and Mehl M J 2002 *J. Phys. Chem. Solids* **63** 833
- [98] Massalski T B 1987 *Binary Alloy Phase Diagrams* vol 1 2nd printing (Metals Park, OH: American Society for Metals) p 253
- [99] Villars P and Calvert L D *Pearson's Handbook of Crystallographic Data for Intermetallic Phases* vol 2 (Materials Park, OH: ASM International) p 2057
- [100] Lekka C H, Bernstein N, Mehl M J and Papaconstantopoulos D A 2003 *Appl. Surf. Sci.* to be published